Axion Mass Prediction from Adaptive Mesh Refinement Cosmological Lattice Simulations

Joshua N. Benabou,[1,2] Malte Buschmann,[3] Joshua W. Foster,[4,5] and Benjamin R. Safdi[1,2]
[1]Berkeley Center for Theoretical Physics, University of California, Berkeley, California 94720, USA
[2]Theoretical Physics Group, Lawrence Berkeley National Laboratory, Berkeley, California 94720, USA
[3]GRAPPA Institute, Institute for Theoretical Physics Amsterdam, University of Amsterdam, Science Park 904, 1098 XH Amsterdam, The Netherlands
[4]Astrophysics Theory Department, Theory Division, Fermilab, Batavia, Illinois 60510, USA
[5]Kavli Institute for Cosmological Physics, University of Chicago, Chicago, Illinois 60637, USA

(Received 13 January 2025; revised 3 April 2025; accepted 29 May 2025; published 20 June 2025)

The quantum chromodynamics (QCD) axion arises as the pseudo-Goldstone mode of a spontaneously broken Abelian Peccei-Quinn (PQ) symmetry. If the scale of PQ symmetry breaking occurs below the inflationary reheat temperature and the domain wall number is unity, then there is a unique axion mass that gives the observed dark matter (DM) abundance. Computing this mass has been the subject of intensive numerical simulations for decades since the mass prediction informs laboratory experiments. Axion strings develop below the PQ symmetry-breaking temperature, and as the string network evolves, it emits axions that go on to become the DM. A key ingredient in the axion mass prediction is the spectral index of axion radiation emitted by the axion strings. We compute this index in this Letter using the most precise and accurate large-scale simulations to date of the axion-string network leveraging adaptive mesh refinement to achieve the precision that would, otherwise, require a static lattice with $262{,}144^3$ lattice sites. We find a scale-invariant axion radiation spectrum to within 1% precision and find no evidence that the spectral index of radiation evolves with time. Accounting for axion production from strings prior to the QCD phase transition leads us to predict that the axion mass should be approximately $m_a \in (45, 65)$ μeV. However, we provide preliminary evidence that axions are produced in greater quantities from the string-domain-wall network collapse during the QCD phase transition, potentially increasing the mass prediction to as much as 300 μeV.

DOI: 10.1103/6v21-d6sj

The quantum chromodynamics (QCD) axion is currently the subject of a rapidly growing worldwide experimental program [1]. The axion is well motivated because it can explain the dark matter (DM) of our Universe, resolve the strong- CP problem of the neutron electric dipole moment [2–8], and appear in string theory compactifications [9,10]. On the other hand, laboratory experiments for axion DM are notoriously difficult because the mass of the QCD axion particle is currently unknown to within roughly 10 orders of magnitude; many axion laboratory experiments and astrophysical probes, in contrast, need to know the axion mass to roughly one part in a million. This work aims to accelerate the search for axion DM by predicting the QCD axion DM mass in the cosmological scenario where the axion is generated as a pseudo-Goldstone boson from a spontaneously broken U(1) symmetry—the Peccei-Quinn (PQ) symmetry—at temperatures below the inflationary reheating temperature (see [11,12] for reviews).

The axion field a would be massless but for its interactions with QCD of the form $\mathcal{L} \supset (g^2/32\pi^2 f_a) a G^a_{\mu\nu} \tilde{G}^{a\,\mu\nu}$, with g the strong coupling constant and G the QCD field strength. This operator generates an axion mass $m_a \approx 5.7(10^{12}\ \mathrm{GeV}/f_a)\mu\mathrm{eV}$ [13] at temperatures below the QCD phase transition. The parameter f_a is the axion decay constant, which is related to the vacuum expectation value (VEV) of the complex scalar that undergoes $U(1)_{\mathrm{PQ}}$ symmetry breaking. Let us denote that complex scalar field as $\Phi = [r + (v_a/\sqrt{2})]e^{ia/v_a}$, where r is a real scalar degree of freedom referred to as the radial mode, and v_a is the VEV of Φ in the broken phase. The VEV v_a and f_a are related by $f_a = v_a/N_{\mathrm{dw}}$, with N_{dw} the domain wall number (dw). In this Letter, we restrict to $N_{\mathrm{dw}} = 1$ to avoid long-lived domain walls. In the thermal universe, the PQ symmetry is restored at high temperatures, such that for $T \gg f_a$ the VEV is $\langle|\Phi|^2\rangle = 0$. The Universe undergoes a phase transition at $T \sim f_a$, where $|\Phi|^2$ acquires a VEV. By the Kibble-Zurek mechanism [14,15], a defect network consisting of axion strings develops for temperatures below that

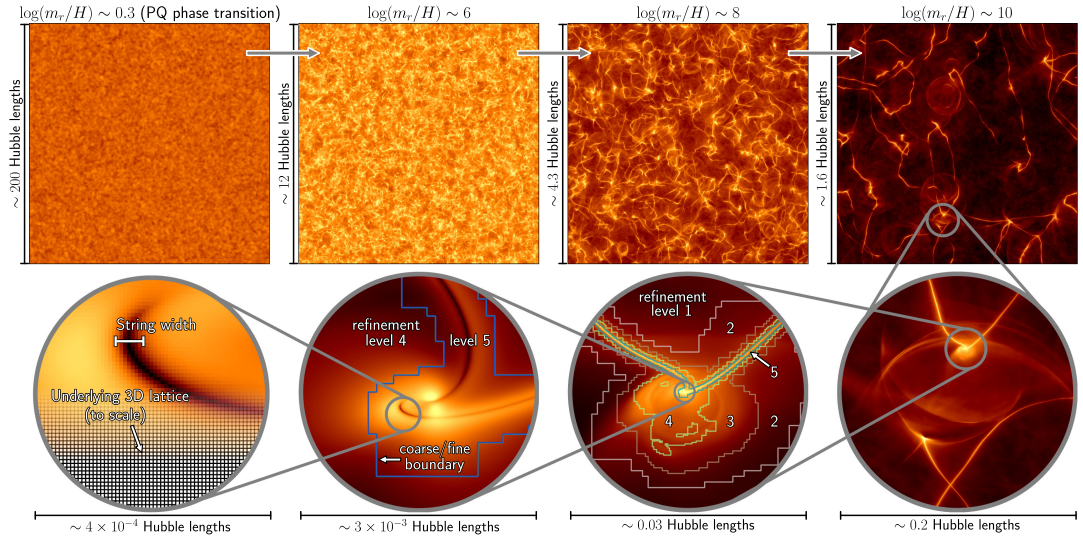

FIG. 1. 3D → 2D projections of the axion energy density on a logarithmic color scale. Each top row panel covers the entire simulation volume at different times, starting at the PQ phase transition (left) to the final state (right). The bottom row is a set of nested zoom-ins of the final state at $\log(m_r/H) \sim 10$ illustrating the large scale separation between the size and width of the strings that make the AMR technique necessary. Overlaid in the three bottom left panels are the refinement boundaries along the line of sight. Animations are available here [18].

of the PQ phase transition. The string network evolves to a scaling solution [16], with roughly a constant number of strings per Hubble patch—up to logarithmic corrections [17]—for temperatures $T < f_a$. At low temperatures, the radial mode is frozen everywhere at its VEV except in the vicinity of the string cores. In Fig. 1, we illustrate the axion-string network in a snapshot of one of our simulations.

The axion-string network persists in the scaling regime until the QCD phase transition at $T \sim 200$ MeV [19]. (Note that the QCD transition is a crossover transition and not a real phase transition [19], though we refer to it as a phase transition in this Letter since the difference is not relevant for our discussion, which is only sensitive to the temperature dependence of the QCD axion mass.) The axion-string network maintains the scaling solution by radiating energy mostly in the form of axions (but see [20–26]). The axions are relativistic until the QCD phase transition. At this point, the rapidly rising axion mass renders them nonrelativistic, and thereafter, they act as cold DM. Also, at the QCD phase transition, domain walls develop between the strings, but with $N_{\rm dw} = 1$ the string-wall network collapses promptly. (See [27–33] for $N_{\rm dw} > 1$.)

To date, significant effort has been dedicated to simulating the axion-string network in order to compute the axion DM abundance and, in turn, the axion mass that leads to the observed amount of relic DM [16,17,34–53]. On the other hand, recent simulations by different groups dramatically disagree on the predicted axion mass. In particular, Refs. [48,51,53] claim that the spectrum of axion radiation emitted by strings becomes infrared (IR) dominated at late times, which leads to a large DM abundance. For example, Ref. [48] finds that the correct DM abundance is achieved for $m_a > 500$ μeV. On the other hand, Ref. [50] found a nearly conformal spectrum of axion radiation, leading to the prediction $m_a \in (40, 180)$μeV. Reference [48] performed a suite of static cosmological lattice simulations of the classical equations of motion for the PQ field in comoving coordinates with lattices up to $4,500^3$ sites, evolving to temperatures as low as $\log(m_r/H) \sim 8$, where m_r is the radial-mode mass and H is the Hubble parameter. (As explained precisely below, $\log(m_r/H)$ is a proxy for time in logarithmic units between the PQ and QCD phase transitions.) More recently, Ref. [52] performed larger static lattice simulations and considered a number of possible models for the time-evolution of the axion emission spectrum, finding them to be roughly equally compatible with the data but only some of them predicting IR-dominated emission at late times. In contrast, Ref. [50] used adaptive mesh refinement (AMR) simulations, with a dynamical lattice that tracks the string cores, to evolve out to $\log(m_r/H) \sim 9$.

In this Letter, we extend the methodology developed in [50] by performing the largest AMR simulation of the axion-string network to date, evolving the network to $\log(m_r/H) \sim 10$; a static lattice would need $262\,144^3$ grid sites to achieve the same resolution as our AMR configuration. Evolving a larger simulation box to lower temperatures both shrinks the statistical uncertainties on the measured quantities and, more importantly, allows us to reach deeper into the scaling regime. This minimizes the systematic uncertainties related to the finite IR and UV cutoffs as well as transients from the PQ phase transition. Additionally, we perform a suite of systematic simulations to account for axion production during the network

collapse and to study the dependence of our results on the initial conditions. We conclude that the axion radiation spectrum shows no sign of becoming IR-dominated at late times and that the spectrum is nearly conformal, with a spectral index consistent with unity to 1% precision. On the other hand, our simulation of the string-wall network collapse during the QCD phase transition suggests that axion production from domain walls, even in the $N_{\rm dw} = 1$ scenario, could dominate over axion production by strings by a factor of a few, which would have dramatic implications for axion direct detection.

PQ epoch simulations—We solve the equations of motion of the complex scalar field Φ on a three-dimensional grid with AMR. (See Appendix A and Supplemental Material (SM) [54] for the equations of motion and simulation details.) We use the publicly available code SLEDGEHAMR [59] to perform one large, primary simulation and, then, a suite of systematic simulations.

We start our primary simulation well before the PQ phase transition with an initial state based on a thermal distribution. More precisely, we define a reference time t_1 such that $H(t_1) = f_a$, where H is the Hubble parameter. Our simulations are evolved in terms of a rescaled conformal time $\eta = R(t)/R(t_1)$, with R the scale factor; in these units, we start our simulation at $\eta = \eta_i = 0.1$. We design our simulations such that the PQ phase transition occurs at $\eta \approx 0.75$.

We explicitly simulate the PQ symmetry breaking of Φ such that axion strings emerge dynamically within our simulation. Note that this approach differs from simulations performed by some other groups (see, e.g., [17,48,52]), where their simulations start after the PQ symmetry is already broken and include a preevolution stage to approach the attractor solution. In SM [54], we show simulation results using this alternate initial condition procedure. At late times, we find no difference between the two approaches. To avoid biases from transient effects at the PQ phase transition, we only analyze the emission spectrum at scale separations larger than $\log(m_r/H) \sim 7.6$, with $m_r = \sqrt{2} f_a$.

All simulations are performed in comoving coordinates. The simulation volume of our fiducial simulation is chosen large enough to avoid finite volume effects until $\log(m_r/H) \sim 10$. The coarse level resolution at the final state is $8,192^3$ cells with five levels of 2× refinement. At $\eta_i = 0.1$, the simulation box contains $2,000^3$ Hubble volumes of comoving length $R(\eta_i)H(\eta_i)$, while this number drops to 200^3 at $\eta = 1$. Our simulation ends at $\eta_f \sim 110$ with approximately 6 Hubble volumes. Our AMR setup ensures that all parts of the simulation volume are resolved, including the string emission wherever required. In particular, string cores at rest are resolved at all times by at least four grid cells.

Our axion mass prediction requires the extraction of two quantities from our primary simulation: (1) the string length per Hubble volume ξ; and (2) the instantaneous emission spectrum $F(k/H)$. We define the total string length per Hubble volume at time t as $\xi = \ell t^2/\mathcal{V}$, where ℓ is the total string length within the simulation volume $\mathcal{V}$. We numerically extract ℓ from our simulation through the algorithm described in [60]. The result is shown in Fig. 2, where data points are separated by a Hubble time [$\Delta \log(m_r/H) = \log 2$] to avoid correlations.

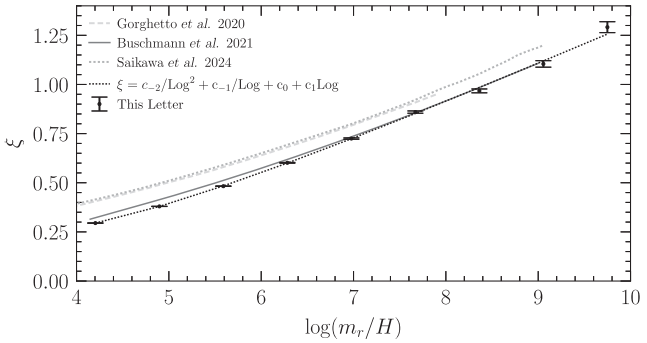

FIG. 2. String length per Hubble volume ξ as a function of the scale separation $\log(m_r/H)$. We compare our result with that of Buschmann *et al.* [50], Gorghetto *et al.* [48], and Saikawa *et al.* [52]. While the simulations may differ at small values of $\log(m_r/H)$ due to differences in the initial state, they all approach the same attractor solution at large $\log(m_r/H)$. We also show a polynomial fit to our data (dotted black curve).

We overlay our result with that of previous simulations [48,50,52], to illustrate that they all approach the same attractor solution [17,48] where ξ linearly increases with the scale separation $\log(m_r/H)$ at late times. The differences at small $\log(m_r/H)$ are due to the differences in the initial state, but this matters very little at large $\log(m_r/H)$, as verified in SM [54] using alternate initial states. We verify the linear increase of ξ by fitting a model of the form $\xi = c_{-2}/\mathrm{Log}^2 + c_{-1}/\mathrm{Log} + c_0 + c_1 \mathrm{Log}$ for $\mathrm{Log} \geq 4$, where $\mathrm{Log} \equiv \log(m_r/H)$. We find $c_1 = 0.21 \pm 0.02$, which is similar to the $c_1 = 0.24 \pm 0.02$ of Gorghetto *et al.* [48], $c_1 = 0.254 \pm 0.002$ of Buschmann *et al.* [50], and $c_1 = 0.23 \pm 0.06$ of Saikawa *et al.* [52]. Note that our linear growth with $\log(m_r/H)$ may be in some tension with the analytic velocity one-scale models [22,61–63], which predict ξ saturating at approximately 1.2, whereas we observe $\xi = 1.29$ by $\log = 9.75$ (but see [64,65] for versions of these models with time-varying tension).

We extrapolate our result to the beginning of the QCD phase transition at $\mathrm{Log}_* \in (60, 70)$ and obtain $\xi_* \in (11, 15)$. More precisely, we define quantities such as ξ_* to be the values at the time t_* defined by $3H(t_*) = m_a(t_*)$, with $m_a(t)$ the time-dependent QCD axion mass.

Now, we turn to the computation of the instantaneous emission spectrum $F(k/H)$. The function F is defined such that $F \propto (1/R^3)\partial_t(R^3 \partial_k \rho_a)$, with ρ_a the axion energy density in momentum space (see, e.g., [17,50]). The

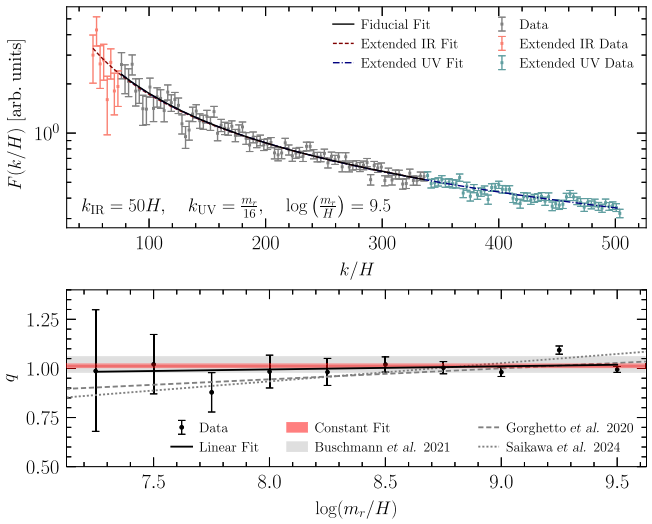

FIG. 3. Top: example of the emission spectrum calculated at $\log(m_r/H) = 9.5$ with associated power-law fit. The best-fit emission spectrum associated with our fiducial analysis choices with $x_{\rm IR} = 50$ and $x_{\rm UV} = 1/16$ is shown in black with the associated data points and inferred error bars shown in gray. Extending the fitting range by taking $x_{\rm IR} = 30$ ($x_{\rm UV} = 1/12$) results in the fit and error bars in red (blue). Bottom: the best-fit emission spectrum index using our fiducial fitting region over an interval between $\log(m_r/H) = 7.25$ and $\log(m_r/H) = 9.5$. The red band illustrates the 1σ containment interval for the constant q model from this Letter, and may be compared with the analogous containment interval from [50] in gray. We also show the best fit to the linear growth in the emission spectrum with $\log(m_r/H)$ in black, along with the best-fit linear growth models of [48] and [52].

function F is important because while ρ_a itself may be determined simply by energy conservation arguments, given the scaling solution for ξ, the spectrum F is needed to compute the number density of axions n_a. In particular, ignoring the effects of the axion mass for a moment, the number density of axions created by the string network at the time t_* may be estimated by (see, e.g., [17,50]) $n_a^* \approx 8\pi f_a^2 H_* \mathrm{Log}_* \xi_* \langle H/k \rangle$, with the expectation value taken with respect to the instantaneous spectrum F at t_*, in the limit of large Log_*. We numerically determine F from our simulation following the procedure described in Appendix D, similar to that of [50]. In particular, note that the magnitude and k dependence of the uncertainties on the data points are assigned hyperparameters that are profiled over in the analysis. In Fig. 3 (top panel), we illustrate the instantaneous spectrum at $\log(m_r/H) = 9.5$, with the time value referring to the earlier time used in the finite difference.

For $1 \ll k/H \ll m_r/H$, we expect $F \propto (k/H)^{-q}$ for some index q, since there is no other mass scale to influence the spectrum. We fit this model to the data for $x_{\rm IR} H < k < x_{\rm UV} m_r$. In our fiducial analysis, we chose $x_{\rm IR} = 50$ and $x_{\rm UV} = 1/16$, as in Ref. [50], to ensure that our fit is performed sufficiently far from the UV and IR cutoffs. In the bottom panel of Fig. 3, we show our best-fit q values at each of the time steps.

We fit two models to the data for q as a function of $\log(m_r/H)$: a linear model, where $q(t) = q_1 \log(m_r/H) + q_0$, and a constant model where $q(t) = q_0$. In the linear fit, we find $q_1 = 0.015 \pm 0.023$, meaning that we find no evidence for a log-varying spectral index even though our data allow for q_1 as high as ~ 0.04 at 1σ confidence. The constant fit returns an index consistent with a conformal spectrum to 1% precision: $q_0 = 1.01 \pm 0.01$ and consistent with [50].

In contrast to our results, many works have found evidence for a logarithmically increasing spectral index q. For example, using a suite of static lattice simulations, Ref. [52] finds $q_1 = 0.093 \pm 0.005$ when fitting a model that grows linear in the log; this disagrees with our result by more than 3 standard deviations. Reference [48] also used a suite of static lattice simulations to find logarithmic growth in q, with $q_1 = 0.053 \pm 0.005$. Both Refs. [48] and [52] use a similar methodology, and we believe that there are several possibilities for how their results could be biased to mimic logarithmic growth in q (see, also, the discussion in [50]). While [48,52] use an alternate procedure for constructing the initial conditions, we show, in SM [54], that this is unlikely to be the source of the discrepancy. On the other hand, Refs. [48,52] are more susceptible to finite-lattice-size effects, since the resolution to the string cores is at the level of around one lattice site per core width toward the end of the simulations, given the finite lattice. Perhaps most importantly, we show, in SM [54], that we can recreate the logarithmic growth seen in [48,52] by choosing less conservative values for the UV cutoff $x_{\rm UV}$.

Axion mass prediction—Previous works such as [48,50,52] have calculated the axion relic DM abundance by accounting for axions produced prior to the QCD phase transition at some reference time defined by, for example, the condition $H(t) = m_a(t)$ in [48,52], or $3H(t_*) = m_a(t_*)$ in [50]. Here, we adopt the latter definition of t_*, though we stress that both choices are somewhat arbitrary since the string network still exists for t larger than these characteristic times. While it is true that the network begins to collapse for $t > t_*$ and is fully gone within a few Hubble times, as we argue below, the axions produced during network collapse can still substantially affect the DM abundance.

If the axion field is in the linear regime, then we can simply estimate the DM abundance by computing the number density in axions at $t = t_*$ and redshifting this number density down to today, leading to the prediction [50]

$$\Omega_a^{\rm str} \approx 0.12 h^{-2} \left(\frac{f_a}{1.4 \times 10^{11}\ \mathrm{GeV}} \right)^{1.17} \frac{318}{\delta} \sqrt{\frac{\xi_*}{13}} \frac{\mathrm{Log}_*}{70} \qquad (1)$$

Here, we assume $m_a^2(T) \propto T^{-8.16}$ [66] along with the number of entropy degrees of freedom $g_*(T) \approx g_*^0 (T/\mathrm{MeV})^\gamma$ for

$800 < T < 1800$ MeV and $g_*^0 \approx 50.8$, $\gamma \approx 0.053$ [67]. The quantity δ, which is a constant that must be determined from simulations, is defined by [50] (for $q > 1$) $\langle H/k \rangle^{-1} \equiv \delta\sqrt{\xi}$, where the expectation value is taken with respect to the instantaneous spectrum F. The reason this quantity is expected to depend on $\sqrt{\xi}$ is because as ξ increases logarithmically with time, the strings necessarily become smaller, such that the IR cutoff of the spectrum moves toward the UV like $\sqrt{\xi}$. We follow [50] and compute $\langle H/k \rangle$, at a given time step, by numerically integrating over k with the simulation output for F for $0 \leq k \leq x_{\rm IR} H$. For larger values of k (assuming $q \geq 1$), we integrate to the physical UV cutoff assuming a fixed choice of q.

In the constant model for $q(t)$, our maximum allowed choice of q at 1σ uncertainty is $q = 1.02$, while our minimal value is $q = 1.00$; lower values of q lead to less DM. For an exactly conformal spectrum, one can show that we should, instead of having a static δ value, write $\delta = \delta_1 {\rm Log}_*$ [50]. As we discuss in SM [54], for $q = 1.02$, we measure $\delta \approx 318$, while for $q = 1.00$, we measure $\delta_1 \approx 8.6$. Varying the index q between 1.00 and 1.02 while also adding in the abundance from misalignment (e.g., [12]) gives us the predicted QCD axion mass range $m_a \in (45, 65)\mu$eV to match the observed relic abundance [68]. Crucially, however, this estimate only accounts for axions produced before t_*. [Note that, while we find no evidence for a log-varying $q(t)$, if we consider our best-fit values for q at 1σ significance at the QCD epoch within the context of the log-varying model, we obtain $m_a \in (30, 400)\mu$eV, with the upper limit corresponding to $q \sim 2$ and $\delta \sim 23$ and with the lower limit dominated by the misalignment contribution. We note that the upper limit, here, is rough because it neglects number-changing processes [48], which may be important in this case because $\langle (a/f_a)^2 \rangle \gtrsim 1$ at the QCD epoch for $q \sim 2$.]

For $N_{\rm dw} = 1$, domain walls form shortly after t_* and cause the string-domain-wall network to collapse by a time $t_{\rm coll} \sim 5 t_*$ (see SM [54]). For $t > t_*$, it is important to account for axions produced both by strings and by the domain walls that stretch between them. To help compute the number of axions produced after t_*, we perform a simulation of the network collapse during the QCD phase transition with an AMR simulation based on an intermediate state of the PQ simulation performed in [50]. (See Appendix C for details.) This simulation begins at $\eta = 0.1$, where the effects of the axion mass should be negligible. A nonzero axion mass is turned on at $\eta \approx 27$, with t_* occurring at $\eta \approx 36$. The simulation ends at $\eta \approx 76$ after the string-wall network has disappeared. In this simulation, we find that the DM abundance increases by a factor of ~ 3 accounting for axions produced after t_* relative to the prediction only accounting for axions produced prior to t_*. However, extrapolating from these results to the physical scenario requires us to analytically understand how the string and domain-wall contributions should scale with ${\rm Log}_*$. We estimate (see SM [54]) that accounting for string production post t_* should increase the DM abundance such that $m_a \in (56, 89)\mu$eV gives the observed DM abundance, while accounting for domain wall production could increase the DM abundance by an additional factor of ~ 5, leading to a mass prediction up to 280 μeV.

Discussion—Future experiments that could achieve sensitivity to QCD axions in the mass range found in this Lettter include MADMAX [69–72], ALPHA [73–75], and DALI [76,77]. On the other hand, we note that our results are still subject to a large systematic uncertainty due to our only rough accounting of axions produced by domain walls, which we find could dominate the DM abundance. Additionally, we note that the axion string cosmology could be more complicated than in the picture assumed in this Letter if, for example, $N_{\rm dw} > 1$ [28,32,78]), or if the axions have a string theory UV completion [79–81]. In particular, our results for the axion emission prior to the QCD phase transition also apply to the $N_{\rm dw} > 1$ scenario, but dedicated simulations would be needed to evolve the network collapse in the QCD epoch in the presence of explicit PQ symmetry breaking in that case.

Acknowledgments—We thank Anson Hook and Tanmay Vachaspati for helpful conversations. We thank Javier Redondo, Kenichi Saikawa, Mark Hindmarsh, and Amelia Drew for their comments on the manuscript. M. B. acknowledges funding from the European Research Council (ERC) under the European Union's Horizon 2020 research and innovation programme (Grant agreement No. 864035). J. W. F. is supported by Fermi Research Alliance, LLC under Contract No. DEAC02-07CH11359 with the U.S. Department of Energy. J. B. and B. R. S are supported in part by the DOE Early Career Grant No. DESC0019225 and in part by the DOE Award No. DESC0025293. This research used resources of the National Energy Research Scientific Computing Center (NERSC), a U.S. Department of Energy Office of Science User Facility located at Lawrence Berkeley National Laboratory, operated under Contract No. DE-AC02-05CH11231 using NERSC Award No. HEP-ERCAP0023978.

Data availability—The data are not publicly available. The data are available from the authors upon reasonable request.

[1] C. B. Adams *et al.*, Axion dark matter, in *Proceedings of the 2022 Snowmass Summer Study* (2022).
[2] R. D. Peccei and Helen R. Quinn, *CP* conservation in the presence of instantons, Phys. Rev. Lett. **38**, 1440 (1977).
[3] R. D. Peccei and Helen R. Quinn, Constraints imposed by *CP* conservation in the presence of instantons, Phys. Rev. D **16**, 1791 (1977).

[4] Steven Weinberg, A new light boson?, Phys. Rev. Lett. **40**, 223 (1978).
[5] Frank Wilczek, Problem of strong p and t invariance in the presence of instantons, Phys. Rev. Lett. **40**, 279 (1978).
[6] John Preskill, Mark B. Wise, and Frank Wilczek, Cosmology of the invisible axion, Phys. Lett. **120B**, 127 (1983).
[7] L. F. Abbott and P. Sikivie, A cosmological bound on the invisible axion, Phys. Lett. **120B**, 133 (1983).
[8] Michael Dine and Willy Fischler, The not so harmless axion, Phys. Lett. **120B**, 137 (1983).
[9] Peter Svrcek and Edward Witten, Axions in string theory, J. High Energy Phys. 06 (2006) 051.
[10] A. Arvanitaki, S. Dimopoulos, S. Dubovsky, N. Kaloper, and J. March-Russell, String axiverse, Phys. Rev. D **81**, 123530 (2010).
[11] Benjamin R. Safdi, TASI lectures on the particle physics and astrophysics of dark matter, Proc. Sci. TASI2022 (**2024**) 009 [arXiv:2303.02169].
[12] Ciaran A. J. O'Hare, Cosmology of axion dark matter, Proc. Sci. COSMICWISPers (2024) 040 [arXiv:2403.17697].
[13] Giovanni Grilli di Cortona, Edward Hardy, Javier Pardo Vega, and Giovanni Villadoro, The QCD axion, precisely, J. High Energy Phys. 01 (2016) 034.
[14] T. W. B. Kibble, Topology of cosmic domains and strings, J. Phys. A **9**, 1387 (1976).
[15] W. H. Zurek, Cosmological experiments in superfluid helium?, Nature (London) **317**, 505 (1985).
[16] Richard Lynn Davis, Cosmic axions from cosmic strings, Phys. Lett. B **180**, 225 (1986).
[17] Marco Gorghetto, Edward Hardy, and Giovanni Villadoro, Axions from strings: The attractive solution, J. High Energy Phys. 07 (2018) 151.
[18] https://tinyurl.com/AxionStringsAMR
[19] Y. Aoki, G. Endrodi, Z. Fodor, S. D. Katz, and K. K. Szabo, The order of the quantum chromodynamics transition predicted by the standard model of particle physics, Nature (London) **443**, 675 (2006).
[20] M. B. Hindmarsh and T. W. B. Kibble, Cosmic strings, Rep. Prog. Phys. **58**, 477 (1995).
[21] Ken'ichi Saikawa, A review of gravitational waves from cosmic domain walls, Universe **3**, 40 (2017).
[22] Chia-Feng Chang and Yanou Cui, Gravitational waves from global cosmic strings and cosmic archaeology, J. High Energy Phys. 03 (2022) 114.
[23] Graciela B. Gelmini, Anna Simpson, and Edoardo Vitagliano, Gravitational waves from axionlike particle cosmic string-wall networks, Phys. Rev. D **104**, 061301 (2021).
[24] Marco Gorghetto, Edward Hardy, and Horia Nicolaescu, Observing invisible axions with gravitational waves, J. Cosmol. Astropart. Phys. 06 (2021) 034.
[25] Joshua N. Benabou, Malte Buschmann, Soubhik Kumar, Yujin Park, and Benjamin R. Safdi, Signatures of primordial energy injection from axion strings, Phys. Rev. D **109**, 055005 (2024).
[26] Naoya Kitajima, Junseok Lee, Kai Murai, Fuminobu Takahashi, and Wen Yin, Gravitational waves from domain wall collapse, and application to nanohertz signals with QCD-coupled axions, Phys. Lett. B **851**, 138586 (2024).
[27] Masahiro Kawasaki, Ken'ichi Saikawa, and Toyokazu Sekiguchi, Axion dark matter from topological defects, Phys. Rev. D **91**, 065014 (2015).
[28] Takashi Hiramatsu, Masahiro Kawasaki, Ken'ichi Saikawa, and Toyokazu Sekiguchi, Axion cosmology with long-lived domain walls, J. Cosmol. Astropart. Phys. 01 (2013) 001.
[29] Andreas Ringwald and Ken'ichi Saikawa, Axion dark matter in the post-inflationary Peccei-Quinn symmetry breaking scenario, Phys. Rev. D **93**, 085031 (2016); **94**, 049908(A) (2016).
[30] E. Armengaud *et al.* (IAXO Collaboration), Physics potential of the international axion observatory (IAXO), J. Cosmol. Astropart. Phys. 06 (2019) 047.
[31] Luca Di Luzio, Maurizio Giannotti, Enrico Nardi, and Luca Visinelli, The landscape of QCD axion models, Phys. Rep. **870**, 1 (2020).
[32] Konstantin A. Beyer and Subir Sarkar, Ruling out light axions: The writing is on the wall, SciPost Phys. **15**, 003 (2023).
[33] Junseok Lee, Kai Murai, Fuminobu Takahashi, and Wen Yin, Induced domain walls of QCD axion, and gravitational waves, J. Cosmol. Astropart. Phys. 10 (2024) 038.
[34] A. Vilenkin and A. E. Everett, Cosmic strings and domain walls in models with Goldstone and PseudoGoldstone bosons, Phys. Rev. Lett. **48**, 1867 (1982).
[35] P. Sikivie, Of axions, domain walls and the early Universe, Phys. Rev. Lett. **48**, 1156 (1982).
[36] Diego Harari and P. Sikivie, On the evolution of global strings in the early Universe, Phys. Lett. B **195**, 361 (1987).
[37] E. P. S. Shellard, Cosmic string interactions, Nucl. Phys. **B283**, 624 (1987).
[38] R. L. Davis and E. P. S. Shellard, Do axions need inflation?, Nucl. Phys. **B324**, 167 (1989).
[39] C. Hagmann and P. Sikivie, Computer simulations of the motion and decay of global strings, Nucl. Phys. **B363**, 247 (1991).
[40] R. A. Battye and E. P. S. Shellard, Global string radiation, Nucl. Phys. **B423**, 260 (1994).
[41] R. A. Battye and E. P. S. Shellard, Axion string constraints, Phys. Rev. Lett. **73**, 2954 (1994); **76**, 2203(E) (1996).
[42] Masahide Yamaguchi, M. Kawasaki, and Jun'ichi Yokoyama, Evolution of axionic strings and spectrum of axions radiated from them, Phys. Rev. Lett. **82**, 4578 (1999).
[43] Vincent B. Klaer and Guy D. Moore, The dark-matter axion mass, J. Cosmol. Astropart. Phys. 11 (2017) 049.
[44] Alejandro Vaquero, Javier Redondo, and Julia Stadler, Early seeds of axion miniclusters, J. Cosmol. Astropart. Phys. 04 (2019) 012.
[45] Amelia Drew and E. P. S. Shellard, Radiation from global topological strings using adaptive mesh refinement: Methodology and massless modes, Phys. Rev. D **105**, 063517 (2022).
[46] Amelia Drew and E. P. S. Shellard, Radiation from global topological strings using adaptive mesh refinement: Massive modes, Phys. Rev. D **107**, 043507 (2023).
[47] Amelia Drew, Tomasz Kinowski, and E. P. S. Shellard, Axion string source modeling, Phys. Rev. D **110**, 043513 (2024).
[48] Marco Gorghetto, Edward Hardy, and Giovanni Villadoro, More axions from strings, SciPost Phys. **10**, 050 (2021).

[49] Michael Dine, Nicolas Fernandez, Akshay Ghalsasi, and Hiren H. Patel, Comments on axions, domain walls, and cosmic strings, J. Cosmol. Astropart. Phys. 11 (2021) 041.

[50] Malte Buschmann, Joshua W. Foster, Anson Hook, Adam Peterson, Don E. Willcox, Weiqun Zhang, and Benjamin R. Safdi, Dark matter from axion strings with adaptive mesh refinement, Nat. Commun. **13**, 1049 (2022).

[51] Heejoo Kim, Junghyeon Park, and Minho Son, Axion dark matter from cosmic string network, J. High Energy Phys. 07 (2024) 150.

[52] Ken'ichi Saikawa, Javier Redondo, Alejandro Vaquero, and Mathieu Kaltschmidt, Spectrum of global string networks and the axion dark matter mass, J. Cosmol. Astropart. Phys. 10 (2024) 043.

[53] Heejoo Kim and Minho Son, More scalings from cosmic strings, arXiv:2411.08455.

[54] See Supplemental Material at http://link.aps.org/supplemental/10.1103/6v21-d6sj for additional details regarding algorithmic implementation, systematic tests, and joint analytic and numerical study of the string and domain wall emission extrapolated to late times, which includes Refs. [55–58].

[55] Weiqun Zhang, Ann Almgren, Vince Beckner, John Bell, Johannes Blaschke, Cy Chan, Marcus Day, Brian Friesen, Kevin Gott, Daniel Graves, Max P. Katz, Andrew Myers, Tan Nguyen, Andrew Nonaka, Michele Rosso, Samuel Williams, and Michael Zingale, Amrex: A framework for block-structured adaptive mesh refinement, J. Open Source Software **4**, 1370 (2019).

[56] Weiqun Zhang, Andrew Myers, Kevin Gott, Ann Almgren, and John Bell, Amrex: Block-structured adaptive mesh refinement for multiphysics applications, Int. J. High Perform. Comput. Appl. **35**, 508 (2021).

[57] Vincent B. Klaer and Guy D. Moore, Global cosmic string networks as a function of tension, J. Cosmol. Astropart. Phys. 06 (2020) 021.

[58] David I. Dunsky and Marius Kongsore, Primordial black holes from axion domain wall collapse, J. High Energy Phys. 06 (2024) 198.

[59] Malte Buschmann, SLEDGEHAMR: Simulating scalar fields with adaptive mesh refinement, Astrophys. J. **979**, 220 (2025).

[60] Leesa Fleury and Guy D. Moore, Axion dark matter: Strings and their cores, J. Cosmol. Astropart. Phys. 01 (2016) 004.

[61] C. J. A. P. Martins, Scaling properties of cosmological axion strings, Phys. Lett. B **788**, 147 (2019).

[62] M. Hindmarsh, J. Lizarraga, A. Lopez-Eiguren, and J. Urrestilla, Scaling density of axion strings, Phys. Rev. Lett. **124**, 021301 (2020).

[63] José Correia, Mark Hindmarsh, Joanes Lizarraga, Asier Lopez-Eiguren, Kari Rummukainen, and Jon Urrestilla, Scaling density of axion strings in terasite simulations, Phys. Rev. D **111**, 063532 (2025).

[64] Filippo Revello and Gonzalo Villa, Cosmic (super)strings with a time-varying tension, J. Cosmol. Astropart. Phys. 04 (2025) 049.

[65] Masahide Yamaguchi, Cosmological evolution of cosmic strings with time dependent tension, Phys. Rev. D **72**, 043533 (2005).

[66] Sz. Borsanyi *et al.*, Calculation of the axion mass based on high-temperature lattice quantum chromodynamics, Nature (London) **539**, 69 (2016).

[67] Maria Paola Lombardo and Anton Trunin, Topology and axions in QCD, Int. J. Mod. Phys. A **35**, 2030010 (2020).

[68] N. Aghanim *et al.* (Planck Collaboration), Planck 2018 results. VI. Cosmological parameters, Astron. Astrophys. **641**, A6 (2020); 652, C4(E) (2021).

[69] Allen Caldwell, Gia Dvali, Béla Majorovits, Alexander Millar, Georg Raffelt, Javier Redondo, Olaf Reimann, Frank Simon, and Frank Steffen (MADMAX Working Group), Dielectric Haloscopes: A new way to detect axion dark matter, Phys. Rev. Lett. **118**, 091801 (2017).

[70] B. Majorovits *et al.* (MADMAX Interest Group), MADMAX: A new road to axion dark matter detection, J. Phys. Conf. Ser. **1342**, 012098 (2020).

[71] P. Brun *et al.* (MADMAX Collaboration), A new experimental approach to probe QCD axion dark matter in the mass range above 40 μeV, Eur. Phys. J. C **79**, 186 (2019).

[72] B. Ary dos Santos Garcia *et al.*, First search for axion dark matter with a Madmax prototype, arXiv:2409.11777.

[73] Matthew Lawson, Alexander J. Millar, Matteo Pancaldi, Edoardo Vitagliano, and Frank Wilczek, Tunable axion plasma haloscopes, Phys. Rev. Lett. **123**, 141802 (2019).

[74] Mackenzie Wooten, Alex Droster, Al Kenany, Dajie Sun, Samantha M. Lewis, and Karl van Bibber, Exploration of wire array metamaterials for the plasma axion haloscope, Ann. Phys. (Amsterdam) **536**, 2200479 (2024).

[75] Alexander J. Millar *et al.* (ALPHA Collaboration), Searching for dark matter with plasma haloscopes, Phys. Rev. D **107**, 055013 (2023).

[76] J. De Miguel, J. F. Hernández-Cabrera, E. Hernández-Suárez, E. Joven-Álvarez, C. Otani, and J. Alberto Rubiño Martín (DALI Collaboration), Discovery prospects with the dark-photons & axion-like particles interferometer, Phys. Rev. D **109**, 062002 (2024).

[77] Javier De Miguel, A dark matter telescope probing the 6 to 60 GHz band, J. Cosmol. Astropart. Phys. 04 (2021) 075.

[78] Chia-Feng Chang and Yanou Cui, Dynamics of long-lived axion domain walls and its cosmological implications, arXiv:2309.15920.

[79] John March-Russell and Hannah Tillim, Axiverse strings, arXiv:2109.14637.

[80] Joshua N. Benabou, Quentin Bonnefoy, Malte Buschmann, Soubhik Kumar, and Benjamin R. Safdi, The cosmological dynamics of string theory axion strings, Phys. Rev. D **110**, 035021 (2024).

[81] Matthew Reece, Extra-dimensional axion expectations, arXiv:2406.08543.

[82] Malte Buschmann, Joshua W. Foster, and Benjamin R. Safdi, Early-Universe simulations of the cosmological axion, Phys. Rev. Lett. **124**, 161103 (2020).

[83] Olivier Wantz and E. P. S. Shellard, Axion cosmology revisited, Phys. Rev. D **82**, 123508 (2010).

[84] Ciaran A. J. O'Hare, Giovanni Pierobon, Javier Redondo, and Yvonne Y. Y. Wong, Simulations of axionlike particles in the postinflationary scenario, Phys. Rev. D **105**, 055025 (2022).

End Matter

Appendix A: Model Lagrangian and equations of motion—We model the dynamics of axions and associated topological defects with a complex scalar $\mathbf{\Phi}$ in a radiation-dominated background subject to the temperature-dependent potential

$$V(\mathbf{\Phi}) = \left(|\mathbf{\Phi}|^2 - \frac{f_a^2}{2}\right)^2 - \frac{\lambda T^2}{3}|\mathbf{\Phi}|^2 + m_a(T)^2 f_a^2\left[1 - \frac{\sqrt{2}|\mathbf{\Phi}|}{f_a}\cos\mathrm{Arg}(\mathbf{\Phi})\right]. \quad \text{(A1)}$$

Here, f_a is the axion decay constant and $m_a(T)$ is the temperature-dependent axion mass.

We work in conformal time $\eta = R(t)/R(t_1)$ where $R(t)$ is the scale factor at time t, and t_1 is the time when the Hubble expansion rate $H(t_1) = f_a$. We also work in comoving spatial coordinates in units of $1/[R(t_1)H(t_1)]$. Then after decomposing $\Phi = f_a(\psi_1 + i\psi_2)/\sqrt{2}$, we obtain the dimensionless equations of motion

$$\psi_i'' + \frac{2}{\eta}\psi_i' - \overline{\nabla}^2\psi_i + \psi_i\left[\eta^2(\psi_1^2 + \psi_2^2 - 1) + \frac{T_1^2}{3f_a^2}\right] - \frac{\eta^2 m_a(\eta)^2}{f_a^2}\delta_{i1} = 0, \quad \text{(A2)}$$

where primes indicate differentiation with respect to η, the $\overline{\nabla}$ is the Laplacian with respect to our dimensionless comoving coordinates, and the δ_{i1} indicates that this term is only applied to the equations of motion of ψ_1. We take $\lambda = 1$ while the ratio $T_1^2/3f_a^2$ represents a residual physical scale, which we take to have a value of $T_1^2/3f_a^2 = 0.562\,33$. Though this value is unphysical, its effect is only to modify the hierarchy between the time that Φ begins to oscillate and when the PQ symmetry is broken; its contribution to subsequent dynamics is negligible.

Appendix B: Details of the PQ simulation—In our PQ simulations, we may take the axion mass to be negligible by sending $m_a \to 0$. Our PQ simulation volume is a box with sidelength $\bar{L} = 200$, where an overbar indicates a quantity in units of the conformal horizon at time t_1. The simulation is resolved by $8,192^3$ lattice sites at the base resolution and begins at an initial conformal time of $\eta_i = 0.1$, through the PQ symmetry breaking at $\eta \approx 0.75$, and until a final time of $\eta_f \approx 110$ when the simulation contains approximately 6 Hubble volumes. At this time, we reach a maximum scale separation of $\log(m_r/H) \approx 9.75$. Over the course of the simulation, as many as five levels of additional refinement are added. Performing an identically resolved uniform lattice simulation would then require a lattice of size $262\,144^3$ and exabytes of memory.

All simulations were performed at the facilities of the National Energy Research Scientific Computing Center (NERSC). The first part of the primary simulation ran for about 1.5 weeks on the now-retired Cori KNL cluster on up to 2,048 nodes with a total of 139 264 CPU cores, 786 432 CPU threads, and 129 TB of aggregate memory. The second part of the simulation ran for another 1.5 weeks on the new Perlmutter cluster on 256 nodes with a total of 32 768 CPU cores, 65 536 CPU threads, and 131 TB of aggregate memory. The simulation is memory bound, i.e., the number of required nodes is primarily set by the amount of memory they can provide.

Appendix C: Details of the QCD simulation—In simulations of the QCD epoch, which we describe at greater length in SM [54], we can no longer neglect the axion mass. We parametrize it by

$$m_a(\eta) = \frac{f_a}{\mathcal{N}}\left(\frac{\eta}{\eta_\star}\right)^{n/2}, \quad \text{(C1)}$$

where $\eta_\star$ is the conformal time when the domain wall network collapses (typically a factor of 2 in conformal time after axion oscillation), and $\mathcal{N}$ is a ratio parametrizing the hierarchy between the axion decay constant and axion mass at this time. We adopt $n = 6.68$, as previously implemented in [82], from [83], and we choose $\mathcal{N} \approx 19$. (See [84] for the effect of varying n on the axion DM abundance.) We use an intermediate state generated during the primary simulation of [50] as the initial state of our QCD simulation. In particular, this provides an initial state at $\eta \approx 27$ in a simulation volume with $\bar{L} = 120$, which we resolve on a $4,096^3$ base resolution lattice. Even though $m_a(\eta)$ is small at the beginning, we multiply (C1) by the logistic function $1/\sqrt{1 + \exp[-3(\eta - 30)]}$ to ensure a smooth transition from the PQ epoch to the QCD epoch. Domain walls form in these simulations at $\eta \approx 32$ when the axion begins to oscillate, and the simulation concludes after the network has fully collapsed at $\eta \approx 76$. We implement identical refinement criteria in this simulation as in our primary string-only simulation, leading to as many as 5 refinement levels.

The simulation ran on the NERSC Perlmutter cluster using initially 256 nodes for 18 hours (32 768 CPU cores, 65 536 CPU threads, and 131 TB of aggregate memory). Once the string-domain wall network started collapsing, we could reduce the number of required nodes to 128 for another ~3 days of runtime.

Appendix D: Fitting the emission spectrum—We numerically extract the function $F(k/H)$ from the simulation output following the procedure described in detail in [50]. We compute the screened time-derivative of the axion field

$$\dot{a}_{\rm screened}(x) = \dot{a}(x)[1 + r(x)/f_a]^2, \tag{D1}$$

with $r(x)$ being the radial mode. The screening is necessary to remove string cores from $\dot{a}(x)$ as these are singularities in the axion field that, otherwise, would pollute the result. We perform a Fourier-transform of $\dot{a}_{\rm screened}(x)$ to obtain $|\tilde{\dot{a}}_{\rm screened}(k)|^2$ using the data at the lowest resolution. Those data are binned in k with a resolution of $\Delta k = 2\pi/\bar{L}$. Then, we compute F by taking the appropriate finite difference over a time spacing of $\Delta \log(m_r/H) = 0.25$. We include all data with $\log(m_r/H) > 7.25$; this choice requires that we have at least $10k$ points in the fit for q.

We denote the binned instantaneous emission spectrum at time Log_i and physical wave number k_j/H_i by F_{ij}. At each Log_i, we assume the emission spectrum is modeled by a power-law mean and standard deviation of the form

$$\mu_{ij}(\mu, q) = \mu\left(\frac{k_j}{H_i}\right)^q, \qquad \sigma_{ij}(\sigma, p) = \sigma\left(\frac{k_j}{H_i}\right)^p, \tag{D2}$$

so that the likelihood of the data at Log_i given the emission spectrum index q is given by

$$\log \mathcal{L}_i(q) = \max_{\{\mu,\sigma,p\}} \sum_j \Phi[F_{ij}, \mu_{ij}(\mu, q), \sigma_{ij}(\sigma, p)] \tag{D3}$$

after profiling over the nuisance parameters $\{\mu, \sigma, p\}$ where $\Phi(x, \mu, \sigma)$ is the log of the Gaussian probability density function with mean μ and standard deviation σ. For an individual spectrum, we can find the best-fit $\hat{q}$ at Log_i by $\hat{q} = \mathrm{argmax}_q \mathcal{L}_i(q)$. Note that, in future work, it would be interesting to test our approach to uncertainty estimation by performing multiple, otherwise identical, simulations but with different, random initial states and computing the variance in the instantaneous spectra at fixed k/H between the different simulation outputs.

Then, to test the constant q hypothesis, we compute the likelihood of the data as a function of $q_0^{\rm const}$. by

$$\log \mathcal{L}(q_0^{\rm const}) = \sum_i \log \mathcal{L}_i(q_0^{\rm const}). \tag{D4}$$

When we consider the case of a logarithmically growing emission spectrum index, we take

$$q = q_1 \mathrm{Log} + q_0 \tag{D5}$$

and profile over the nuisance parameter q_0 so that we have

$$\log \mathcal{L}(q_1) = \max_{q_0} \sum_i \log \mathcal{L}_i(q_1 \mathrm{Log}_i + q_0). \tag{D6}$$

Then, following standard frequentist treatments [11], we estimate the best-fit constant index $\hat{q}_0^{\rm const}$. by maximizing $\log \mathcal{L}(q_0^{\rm const})$ with 1σ confidence intervals on our estimate of $\hat{q}_0^{\rm const}$. given by $q_0^{\rm const}$. such that $\log \mathcal{L}(\hat{q}_0^{\rm const}) - \log \mathcal{L}(q_0^{\rm const}) = 1/2$. Estimating a best-fit and containment interval for q_1 and/or q_0 follows an identical procedure.

Appendix E: Axion mass prediction—To extract the axion mass, we follow the procedure in Ref. [50]. The number density of axions emitted by the string network at the time of the QCD phase transition, specified by $\log(m_r/H) = \mathrm{Log}_*$, is, for $q > 1$, $n_a^{\rm string} \approx (8\pi f_a^2 H/\delta)\sqrt{\xi_*}\mathrm{Log}_*$, where δ parametrizes $\langle H/k\rangle^{-1} = \delta\sqrt{\xi}$. Recall that, physically, δ encodes the dependence of the effective IR cutoff on the typical interstring separation: $k_{\rm IR}/H \propto \sqrt{\xi}$. Redshifting $n_a^{\rm string}$ down to the present day, the abundance of QCD axion DM receives a contribution from string emission Ω_a^{str} given by (1) [50]. To obtain the total relic abundance, we multiply Ω_a^{str} by a fudge factor $\mathcal{F}$ to account for the axions produced during the QCD phase transition at times $t > t_*$, with t_* defined such that $3H(t_*) = m_a(t_*)$. In Ref. [50], it was assumed that no axions are produced after the time t_* such that $\mathcal{F} = 1$. Following the arguments in SM [54], we take $\mathcal{F} = 1.7$ to account for axion production after t_* from strings and $\mathcal{F} = 8.2$ to account for production after t_* from both strings and domain walls. Note that, when matching the axion relic abundance to the observed DM abundance, we also account for the contribution from misalignment, which we take as [66]

$$\Omega_a = 0.12 h^{-2}\left(\frac{28\ \mu\mathrm{eV}}{m_a}\right)^{1.17}. \tag{E1}$$

The inverse expectation value $\langle H/k\rangle^{-1}$ is shown for our fiducial spectrum fit in Fig. S1 in SM [54]. Recall that for our fiducial emission spectrum, we measure the spectral index to be $q = 1.013 \pm 0.0095$. Assuming the spectral index is at its 1σ upper limit $q = 1.02$, we obtain $\delta = 318.2 \pm 2.1$. In the case of a conformal spectrum $q = 1$, we use (1) to compute the relic abundance from string emission with the replacement $\delta \to \delta_1 \mathrm{Log}_*$. We find $\delta_1 = 8.6 \pm 0.1$. Note that Ref. [50] found $\delta = 113 \pm 7$, for the fiducial spectrum fit to the AMR simulation (for which $x_{\rm IR} = 50$ and $q = 1.06$) and $\delta_1 = 6.2 \pm 0.4$ in the case of a conformal spectrum.

We compute ξ_* assuming that the functional form $\xi = c_{-2}/\mathrm{Log}^2 + c_{-1}/\mathrm{Log} + c_0 + c_1 \mathrm{Log}$, which is fit to the data for $\mathrm{Log} \geq 4$ (see main text), remains valid

until the QCD phase transition. We allow the fit coefficients c_i to vary within their 1σ ranges. Varying $(\mathrm{Log}_*, \xi_*, q)$ with $\mathrm{Log}_* \in (60, 70)$, and q between 1 and its upper limit at 1σ, we obtain the range of axion masses $150 - 280$ μeV. Note that not including any emission from times $t > t_*$ would result in the mass range $45 - 65$ μeV, consistent with Ref. [50], while ignoring the emission from domain walls corresponds to the range 56, 89) μeV.